

Hemispheric Albedo Asymmetries across Three Phases of CMIP[✉]

TRAUTE CRUEGER,^a HAUKE SCHMIDT,^a AND BJORN STEVENS^a

^a *Max Planck Institute for Meteorology, Hamburg, Germany*

(Manuscript received 13 December 2022, in final form 28 March 2023, accepted 29 March 2023)

ABSTRACT: Earth's planetary albedo shows a remarkable hemispheric symmetry. We assess to what extent CMIP models symmetrize the hemispheric clear-sky albedo asymmetry and what the role of clouds is for this. Following Voigt et al., we calculate a reference TOA reflected solar radiation considering the masking of clear-sky asymmetry by symmetric cloud contributions. We use the simple radiation model of Donohoe and Battisti to estimate this benchmark and to separate surface, aerosol, and cloud contributions to the compensation of this benchmark. In CERES, tropical clouds enhance the reference asymmetry while extratropical cloud asymmetries balance the reference asymmetry and the additional asymmetry introduced by tropical clouds. CMIP multimodel means show similar results as CERES. Clouds compensate reference asymmetries by 85% (CMIP3), 65% (CMIP5), and 78% (CMIP6) as compared with 98% for CERES. Spatial distributions of hemispheric differences indicate clear improvements across the CMIP phases. Remaining all-sky reflection asymmetries predominantly result from too-small, partly compensating cloud asymmetries: a too-weak enhancement of the reference asymmetry in the tropical Atlantic and eastern Pacific Oceans is accompanied by a too-weak compensation by extratropical clouds. Thus, tropical clouds and extratropical storm track regions are largely responsible for the compensation of hemispheric clear-sky asymmetries in CERES and CMIP, and for remaining biases in the GCMs. An unexpected result is the magnitude of model biases in the clear-sky asymmetries, which potentially condition systematic cloud biases. Experiments testing cloud-controlling factors influencing hemispheric asymmetry could help us to understand what drives hemispheric cloud differences.

KEYWORDS: Radiation; Aerosols; Albedo; Cloud radiative effects; Satellite observations; General circulation models

1. Introduction

A fundamental parameter of Earth's climate is the planetary albedo (in the following albedo), that is, the fraction of the insolation that is scattered back to space by Earth, measured usually as the ratio of outgoing and incoming solar irradiance at the top of the atmosphere (TOA). Its value is about 0.29 (Vonder Haar and Suomi 1971; Loeb et al. 2009). A curiosity of Earth's albedo is its hemispheric symmetry. Based on the first satellite measurements of Earth's energy budget, Vonder Haar and Suomi (1971) concluded that annual mean differences between outgoing solar radiation in the northern and southern hemispheres were indistinguishable. However, the precision of the instruments at that time only made it possible to rule out differences between the hemispheric albedo larger than 3.5 W m^{-2} , which is a few percent of the mean reflection.

With the advent of the Clouds and the Earth's Radiant Energy System (CERES; Loeb et al. 2002, 2018; Kato et al. 2018) it became possible to measure Earth's albedo with much greater precision. Using 11 years of CERES measurements, Stevens and Schwartz (2012) showed the hemispheric albedo symmetry to be within a few per mill (0.35 W m^{-2}) of the average reflectance. With a more refined analysis,

Voigt et al. (2013) calculated a mean hemispheric difference that was even smaller, that is, 0.1 W m^{-2} , and showed its robustness across several releases (processing improvements) of the CERES data. Additionally, they found that, generally, CMIP3 models do not well represent the symmetry, in line with findings for CMIP5 models presented in a subsequent review by Stephens et al. (2015). Making use of a much longer CERES time series, Datsieris and Stevens (2021) quantified the interannual variability of albedo asymmetry to demonstrate that the hemispheric albedo difference is indistinguishable from zero. Using this longer record, it has also been possible to show that trends in the hemispherically symmetric component of the albedo are much larger than those in the asymmetric component (Datsieris and Stevens 2021; Jönsson and Bender 2022).

This negligible difference, and its stability over time, is surprising because the land surfaces and atmospheric aerosol introduce an asymmetry in the clear-sky reflectance of about 6.15 W m^{-2} (Datsieris and Stevens 2021) and because human activities lead to long-term trends in both quantities (Diamond et al. 2022). These facts, and other statistical properties of the symmetry, led Datsieris and Stevens (2021) and Voigt et al. (2013) to conclude that the observed degree of symmetry is unlikely to arise by chance. However, so far, a physical argument as to what processes act to maintain the symmetry is lacking. While experiments with a single model show a strong influence of the albedo asymmetry on the simulated climate (Haywood et al. 2016), efforts to identify physical arguments are hampered by the fact that models do not, per se, reproduce the observed symmetry (Voigt et al. 2013; Jönsson and Bender 2022) in ways that might be expected if they shared a robust large-scale mechanism. This finding could be taken as indicative that the symmetry

[✉] Supplemental information related to this paper is available at the Journals Online website: <https://doi.org/10.1175/JCLI-D-22-0923.s1>.

Corresponding author: Traute Crueger, traute.crueger@mpimet.mpg.de

does, indeed, arise by chance, a conclusion that would benefit from a more thorough analysis of the models.

The difference of about 6 W m^{-2} between the clear-sky and all-sky hemispheric differences can only be caused by clouds. As shown by Voigt et al. (2014), clouds symmetrize the planetary albedo in two ways. First, they mask surface asymmetries and, second, their asymmetries can compensate any remaining asymmetry. The masking effect is due to the fact that the atmosphere is not cloud-free. In the hypothetical case of a cloud-free atmosphere, the all-sky and the clear-sky asymmetries would be equal. Clouds, however, generally attenuate clear-sky reflection so that hemispherically symmetric clouds would act to reduce the all-sky asymmetry. This represents a masking effect, but not a compensation process, because clouds do not respond to the clear-sky asymmetries. A compensation process can only be assumed, if clouds adjust, that is, become hemispheric asymmetric in order to compensate the remaining masked asymmetry.

The masking of surface albedo contributions to planetary albedo by clouds has been discussed in a large number of studies (e.g., Qu and Hall 2005; Donohoe and Battisti 2011; Voigt et al. 2014; Stephens et al. 2016; Haywood et al. 2016). Donohoe and Battisti (2011), Stephens et al. (2015), and Loeb et al. (2019) estimated the surface and atmosphere contributions to the planetary albedo and the TOA outgoing shortwave (SW) radiation using slightly different variants of a one-layer atmosphere model. With this approach, Donohoe and Battisti (2011) estimated that the global mean surface albedo of 0.123 contributes only 0.036 to the planetary albedo. That is, given the planetary albedo of 0.298, the contribution of the surface to the planetary albedo is only about 12%, as compared with 88% from the atmosphere. This framework for separating cloud and atmospheric from surface contributions has, however, not been systematically employed to quantify cloud compensation effects on the hemispheric albedo symmetry.

Voigt et al. (2014) adopted a different approach to test possible compensation mechanisms by clouds. By varying the surface albedo in simulations with a slab-ocean aqua-planet configuration of a GCM, they showed that the intertropical convergence zone (ITCZ) shifts toward the hemisphere with the darker surface, that is, with the smaller albedo, to partly compensate the effect of the varying surface albedo. Although the importance of the high-latitude storm tracks for the planetary albedo has long been appreciated (Arrhenius 1896; Vonder Haar and Suomi 1971; Donohoe and Battisti 2011), Datseris and Stevens (2021) concluded that extratropical clouds, rather than shifts in the ITCZ rainbands, act to compensate the observed hemispheric asymmetry of clear-sky reflected solar radiation. Jönsson and Bender (2022) showed that the same is true for the subset of CMIP models they analyzed.

In the present study, we build on past work to more thoroughly explore to what extent general circulation models (GCMs) capture the observed albedo symmetry and its decompositions in space and time. Voigt et al. (2013) analyzed CMIP3 models. They identified a tendency of a few models to overcompensate for the clear-sky asymmetry and concluded that the models do not reliably capture the hemispheric

symmetry. Stephens et al. (2015) came to a similar conclusion based on CMIP5 models. These studies, however, only explored hemispheric averages of surface and atmosphere contributions to the TOA-reflected radiation and did not distinguish masking and compensating contributions by clouds. Recently, Jönsson and Bender (2022) evaluated the ability of a subset (selected by the availability of output data) of 11 CMIP6 models to represent drivers of hemispheric albedo asymmetry, its year to year variability, and trends. They found that the variability and trends in the simulated albedo asymmetry were generally larger than observed and explained by variability in the tropics; however, the asymmetry itself was best explained by asymmetries in extratropical clouds. In our study, we focus more on assessing to what extent simulated clouds compensate versus mask cloud-free albedo asymmetries, and on the regional contributions to this compensation. We also analyze if the simulation of the albedo symmetry has improved from CMIP3 over CMIP5 to CMIP6.

After introducing the observational data and model output used in this study and describing the methods in section 3, we present the results for the CERES satellite data (section 4a) that are used as a reference to evaluate model simulations of the three CMIP phases (section 4b). Section 5 includes a discussion and summary of the main results of this study.

2. Data

We analyze output of GCMs that participated in three major phases of CMIP, namely, CMIP3 (Meehl et al. 2007), CMIP5 (Taylor et al. 2012), and CMIP6 (Eyring et al. 2016). The simulations were performed in the so-called historical setup, that is, the CO_2 emissions, the aerosol burden, solar irradiation, and orbital parameters are prescribed according to historical estimations. The investigation periods for the three CMIP phases differ by a couple of years (1980–99 for CMIP3, 1986–2005 for CMIP5, and 1995–2014 for CMIP6), leading to slight differences in the prescribed conditions. The GCMs analyzed for this study are listed in Tables S1–S3 in the online supplemental material. These represent the entire group of GCMs for which historical simulations and the necessary output are available. Generally, the necessary model output is provided only for one realization of the individual GCMs (see section 3). Thus, only one realization for all individual GCMs is utilized. As a reference, we use edition 4 of the CERES–EBAF (CERES–EBAF–Ed4.0) surface and TOA satellite data for the period of 2001 to 2016 (Kato et al. 2018; Loeb et al. 2018). The CERES clear-sky TOA fluxes represent cloud-free areas in contrast to the clear-sky fluxes of most of the GCMs, whose grid boxes are cloud-cleared. For SW fluxes, biases from these different derivations can be neglected (CERES_EBAF_Ed4.0/17/2018 Data Quality Summary, 17 January 2018, downloaded from https://ceres.larc.nasa.gov/documents/DQ_summaries/CERES_EBAF_Ed4.0_DQS.pdf on 31 January 2023). For CERES and all GCMs investigated here, data are provided as monthly means. Before the analysis, all data were interpolated onto a regular grid with 192×96 grid points at a distance of 1.875° . In addition, temporal averages of the data were calculated.

3. Methods

As mentioned in section 1, we investigate the extent to which clouds compensate the masked clear-sky asymmetry. Thus, first, the cloud masking effect has to be estimated. For that reason, we calculate a reference TOA SW upward radiation following the approach of Voigt et al. (2014), who introduced such a benchmark to assess cloud compensation effects in their idealized model simulations. In their study, the authors used cloud cover symmetrized with respect to the equator as an attenuation factor for clear-sky radiation. Here, we adjust this approach by introducing an attenuation factor calculated by surface contributions to the TOA SW upward radiation to estimate the reference reflection. This approach is energetically consistent, in contrast to the use of cloud fraction. The radiation components needed for our reference reflection are obtained following Donohoe and Battisti (2011), who developed a simple radiation model with the basic assumption that the total TOA SW upward radiation F at each grid point can be decomposed into contributions from the atmosphere, F_{atm} , and from the surface, F_{srf} (note that we omit zonal and meridional indices in the following equations):

$$F = F_{\text{srf}} + F_{\text{atm}}. \quad (1)$$

Donohoe and Battisti (2011) further assumed that for each pass through the atmosphere, certain constant proportions of the incident radiation are absorbed and reflected, respectively. Given that an infinite number of reflections can occur, Donohoe and Battisti (2011) derived their Eqs. (1)–(5), which we reformulate to obtain an equation for F_{atm} :

$$F_{\text{atm}} = \frac{F - \alpha_0 \mathcal{T}_{\text{atm}}^2 S}{1 - (\alpha_0 \mathcal{T}_{\text{atm}})^2}, \quad (2)$$

where S is the insolation and α_0 and \mathcal{T}_{atm} are the surface albedo and atmospheric transmissivity, respectively. These are respectively defined from S , its value at the surface¹ (S_0^\downarrow), and how much is reflected by the surface (S_0^\uparrow) such that

$$\mathcal{T}_{\text{atm}} = S_0^\downarrow / S \quad \text{and} \quad \alpha_0 = S_0^\uparrow / S_0^\downarrow. \quad (3)$$

According to Eq. (1), F_{srf} can be obtained as the difference between F and F_{atm} . We can compute the clear-sky counterparts to the all-sky top-of-atmosphere fluxes using the above formulation applied to results from cloud-free radiative transfer computations; these are denoted by G . Cloud contributions are then defined as the difference between the all-sky and the cloud-free-sky values; for instance, the cloud contribution to the atmospheric component of the outgoing flux at the top of the atmosphere is given by $F_{\text{atm}} - G_{\text{atm}}$.

To estimate \tilde{F} , which we define as the value that F would have if only the hemispherically symmetric contribution of clouds were considered, we have to separate cloud and clear-

sky contributions in Eq. (1) and then symmetrize the cloud contributions. To do so, we introduce a factor γ that quantifies the attenuation of the surface contribution through clouds by the ratio between TOA SW reflection from the surface (F_{srf}) and that assuming clear-sky conditions (G_{srf}):

$$\gamma = F_{\text{srf}} / G_{\text{srf}}. \quad (4)$$

A similar factor obtained from the ratio $F_{\text{atm}} / G_{\text{atm}}$ would not describe the cloud contribution to the atmospheric contribution properly because F_{atm} contains the radiation reflected by clouds (which we call F_{cld}) and the radiation reflected by aerosols, which can be attenuated by clouds. Under the assumption that aerosols are predominantly located below clouds, this latter attenuation can be described by the same factor γ , whereby

$$F_{\text{atm}} = F_{\text{cld}} + \gamma G_{\text{atm}}. \quad (5)$$

In contrast to F_{cld} , $F_{\text{atm}} - G_{\text{atm}}$ does not contain the total contribution of cloud reflection but only that part of the irradiance that would not be reflected by aerosols due to the attenuation by clouds in the same column. Inserting Eqs. (4) and (5) into Eq. (1) gives

$$F = \gamma G_{\text{srf}} + F_{\text{cld}} + \gamma G_{\text{atm}} = F_{\text{cld}} + \gamma G. \quad (6)$$

Now, we assume that the effects of clouds on radiation are hemispherically symmetric, while all other components remain unchanged. Then, from Eq. (6) we obtain the benchmark TOA SW reflection \tilde{F} :

$$\tilde{F} = \bar{F}_{\text{cld}} + \bar{\gamma} G, \quad (7)$$

with the bar as a symbol for the symmetric component of an arbitrary variable A :

$$\bar{A}(\lambda, \varphi) = \frac{1}{2} [A(\lambda, \varphi) + A(\lambda, -\varphi)], \quad (8)$$

for any latitude φ and longitude λ . This gives the hemispheric asymmetry of \tilde{F} as

$$\Delta \tilde{F} = \bar{\gamma} \Delta G, \quad (9)$$

with Δ indicating the difference between corresponding quantities in the Northern and Southern Hemispheres. The reference asymmetry $\Delta \tilde{F}$ yields the benchmark to assess whether clouds do not only attenuate (or mask) but also adjust to compensate the hemispheric clear-sky asymmetry. A compensation of the clear-sky asymmetry by asymmetric cloud contributions can only be assumed when the all-sky hemispheric difference ΔF is below $\Delta \tilde{F}$.

In the following, we will use the notation $\mathcal{T}(\lambda, \varphi)$ to denote any irradiance (e.g., F , or G_{atm}) varying in longitude λ and latitude φ ; $\mathcal{T}(\varphi)$ denotes a zonal average. Respective differences between the Northern and Southern Hemispheres are given by the Δ operator, so, for instance, ΔG_{srf} denotes the difference in the hemispherically averaged surface contribution to the clear-sky shortwave irradiance at the top of the

¹ Values at the surface are denoted by subscript 0, whereas contributions to values at the top of the atmosphere from the surface are denoted by subscript “srf.”

TABLE 1. Variables, operators, and abbreviations used in this study.

Symbol/ operation	Meaning
S	Insolation at top of atmosphere
S_0^{\downarrow}	Downwelling shortwave irradiance at surface
S_0^{\uparrow}	Upwelling shortwave irradiance at surface
F	Upwelling irradiance at top of atmosphere
G	Cloud-free value of F
F_{atm}	Atmosphere contribution to F
G_{atm}	Atmosphere contribution to G
F_{srf}	Surface contribution to F
G_{srf}	Surface contribution to G
\bar{F}	F if cloud contributions were symmetric
α_0	Surface albedo
γ	Attenuation factor of clear-sky surface reflection by clouds
$\Delta\mathcal{F}$	Hemispheric difference (NH – SH) of the irradiance \mathcal{I}
$\bar{\chi}$	Symmetric value of field χ w.r.t. the equator
φ	Latitude ($^{\circ}$)
λ	Longitude ($^{\circ}$)
NH	Northern Hemisphere
SH	Southern Hemisphere

atmosphere. The upward shortwave irradiance at the TOA is generally called reflected radiation. To symmetrize the data for the calculation of the reference reflection hemispheric difference ($\Delta\bar{F}$), we assumed that clouds are equally distributed over the globe. Table 1 summarizes the abbreviations used in this article.

4. Results

First, we use the framework of Donohoe and Battisti (2011) as described above to identify contributions to the TOA SW outgoing (reflected) radiation for the CERES satellite data and thereby provide a reference for the model evaluation that follows. We concentrate on differences between the Northern and Southern Hemispheres in terms of zonal and hemispheric mean values, and, additionally, regional patterns.

a. CERES data

1) HEMISPHERIC AVERAGES AND LATITUDE DEPENDENCE

Consistent with the findings of Donohoe and Battisti (2011), Stephens et al. (2015) and Jönsson and Bender (2022), our analysis shows that F_{atm} provides the dominant contribution to F and balances the hemispheric asymmetry associated with F_{srf} . Fig. 1 shows the zonal mean hemispheric differences for the satellite data. Table 2 shows the hemispheric mean differences (see Table S4 in the online supplemental material for the differences for selected difference bands). The zonal mean hemispheric difference of the total reflected radiation [$\Delta F(\varphi)$] is positive in the tropics with a peak around 5° , close to zero at 15° , again positive until about 45° , and negative poleward with a peak around 70° . This alternating pattern integrates to the hemispheric symmetry as indicated by the hemispheric mean

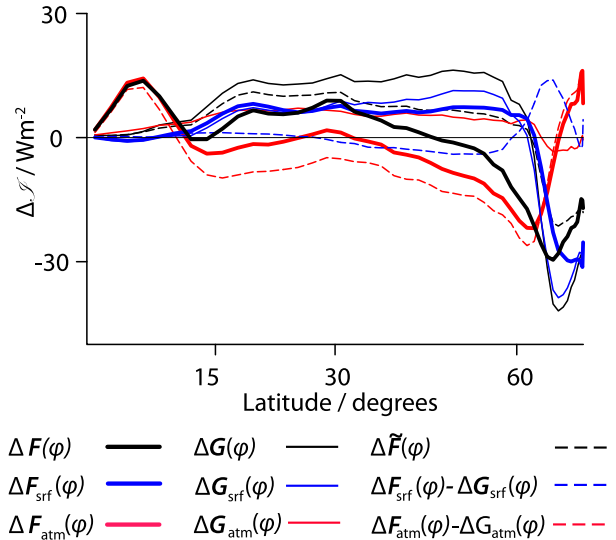


FIG. 1. Zonal mean NH – SH differences of CERES TOA SW upward radiation: all-sky [$\Delta F(\varphi)$], clear-sky [$\Delta G(\varphi)$], all-sky surface [$\Delta F_{\text{srf}}(\varphi)$], all-sky atmosphere [$\Delta F_{\text{atm}}(\varphi)$], reference [$\Delta\bar{F}(\varphi)$], surface clouds [$\Delta F_{\text{srf}}(\varphi) - \Delta G_{\text{srf}}(\varphi)$], and atmosphere clouds [$\Delta F_{\text{atm}}(\varphi) - \Delta G_{\text{atm}}(\varphi)$]. The period that is covered is 2001–16.

difference of only 0.09 W m^{-2} . The clear-sky difference (ΔG) is of 6.15 W m^{-2} . It may seem surprising that the surface contribution (ΔG_{srf}) to this hemispheric difference is only 2.25 W m^{-2} , while a larger contribution of 4.11 W m^{-2} comes from the atmosphere (ΔG_{atm}), that is, from more aerosols in the NH. This is in line with results of Jönsson and Bender (2022) and Diamond et al. (2022), who also demonstrated that hemispheric differences in atmospheric composition (aerosols) contribute twice as much to the clear-sky asymmetry as do hemispheric differences in the distribution and properties of the surface. In the midlatitudes, the largest contribution to the difference actually originates from the surface, that is, a larger fraction of land surfaces in the NH. This is partly compensated by large negative differences at polar latitudes, probably caused by the, on average, larger surface albedo during the Antarctic than during the Arctic summer.

The tropical peak in $\Delta F(\varphi)$ can be attributed clearly to the atmosphere [$\Delta F_{\text{atm}}(\varphi)$] and is dominated by a cloud contribution [$\Delta[F_{\text{atm}}(\varphi) - G_{\text{atm}}(\varphi)]$]. Clear-sky differences [$\Delta G(\varphi)$] are small in this region. However, between about 15° and 60° , the clear-sky contributions to reflected SW radiation $\Delta F(\varphi)$ is much larger in the Northern than in the Southern Hemisphere. As we will show below, larger land surfaces in the north, especially the highly reflective subtropical deserts, provide considerable contributions. In addition, hemispherically asymmetric aerosol loading contributes to the high $\Delta G(\varphi)$ values in this latitude band (see Figs. 2b,d,f). Typically, $\Delta G(\varphi)$ is close to 10 W m^{-2} in this region, with roughly similar contributions from the surface [$\Delta G_{\text{srf}}(\varphi)$] and atmosphere [$\Delta G_{\text{atm}}(\varphi)$]. The $\Delta G_{\text{atm}}(\varphi)$ is approximately compensated by the negative difference in cloud contributions dominated by [$\Delta[F_{\text{atm}}(\varphi) - G_{\text{atm}}(\varphi)]$], such that the total atmospheric contribution to the asymmetry is small, between 15° and around 45° . The negative $\Delta[F_{\text{atm}}(\varphi) - G_{\text{atm}}(\varphi)]$ has its minimum

TABLE 2. Global means and mean hemispheric differences (NH – SH) of CERES TOA SW upward radiation I (W m^{-2}).

	F	G	\bar{F}	F_{srf}	G_{srf}	$F_{\text{srf}} - G_{\text{srf}}$	F_{atm}	G_{atm}	$F_{\text{atm}} - G_{\text{atm}}$
Global mean	99.11	53.30	30.46	12.21	20.81	-8.59	86.88	32.49	54.39
NH – SH	0.09	6.15	3.96	2.25	2.04	0.21	-2.16	4.11	-6.27

around 65° , with a value close to -20 W m^{-2} , and is due to the larger cloudiness in the SH, as pointed out by Datsiris and Stevens (2021). However, the north-minus-south difference in the total radiation [$\Delta F(\varphi)$] has its minimum somewhat more poleward due to increasing contributions from the higher surface albedo as one approaches the South Pole.

Figure 1 also shows the zonal mean hemispheric difference of the reference radiation [$\Delta \bar{F}(\varphi)$], calculated under the assumption of hemispherically symmetric cloud radiative effects. As expected, the shape of $\Delta \bar{F}(\varphi)$ is similar to that of $\Delta G(\varphi)$, but its amplitude is muted. The reference hemispheric mean difference $\Delta \bar{F}$ is 3.96 W m^{-2} , that is, a bit less than two-thirds of ΔG .

2) REGIONAL DISTRIBUTION

To identify regional contributions to the hemispheric flux differences discussed above, Fig. 2 shows north polar projection maps of the CERES $\Delta I(\lambda, \varphi)$. Although only one hemisphere is shown, the signatures of both hemispheres appear in the maps. This is especially evident in Fig. 2d, representing the clear-sky asymmetry from the surface reflection. Because ocean surfaces have similar albedo values, areas where both hemispheres have ocean surfaces (hatched areas) differ negligibly. Over land areas, the picture is different: the, in general, higher reflectance over land than over oceans causes positive differences between the hemispheres where land is covering the NH but ocean covers the SH, and negative differences in the opposite case. Thus, signatures of the Northern Hemisphere land areas appear in red, while the Southern Hemisphere land areas reveal blue colors in Fig. 2. Not only land–ocean contrasts but also land surface contrasts (dotted areas) contribute to the asymmetry. Positive differences occur, for instance, where the eastern part of the Saharan desert is compared with darker, more vegetated surfaces in Africa south of the equator. Generally, however, areas with land in both hemispheres show small values, for example, the American and African land areas near the Equator. Figure 2d further demonstrates the different brightness in the polar areas. The negative values poleward of 60° are a clear signature of the larger brightness in the Antarctic relative to the Arctic. This leads to a considerable compensation of the asymmetry introduced by the land surfaces equatorward of 60° , which has also been found by Diamond et al. (2022).

The atmosphere contribution to the clear-sky asymmetry [$\Delta G_{\text{atm}}(\lambda, \varphi)$], which can be interpreted as an aerosol effect, reveals almost only positive values, dominated by dust emissions from the Sahara over Africa, the Middle East, and the Atlantic, indicative of a more minor role for the anthropogenic aerosol (Fig. 2f). The positive values are partly balanced by sea-salt contributions over the southern ocean. In contrast to these natural sources, anthropogenic effects are supposed

to dominate over Asia with moderate positive values. As shown in Table 2, the contribution from the cloud-free atmosphere sums up to a spatial mean asymmetry of 4.11 W m^{-2} , which dominates the hemispheric clear-sky asymmetry of 6.15 W m^{-2} because of considerable spatial compensation of regionally large positive and negative values of the surface contribution $\Delta G_{\text{srf}}(\lambda, \varphi)$ (Figs. 1 and 2d).

The cloud part of the surface contribution to the reflected radiation, $\{\Delta[F_{\text{srf}}(\lambda, \varphi) - G_{\text{srf}}(\lambda, \varphi)]\}$, shows opposite and clearly smaller amounts than $\Delta G_{\text{srf}}(\lambda, \varphi)$ (Figs. 2d,e). In contrast, the cloud contribution to F_{atm} , $\{\Delta[F_{\text{atm}}(\lambda, \varphi) - G_{\text{atm}}(\lambda, \varphi)]\}$, is much larger in magnitude, indicative of the important role of clouds in controlling planetary albedo (Fig. 2g). Large, positive cloud contributions to the hemispheric differences come from the tropical Pacific and Atlantic regions, as also reflected by the zonal means (Fig. 1), and are related to the mean position of the ITCZ and associated clouds being north of the equator. Likewise, the convective regions over the western boundary currents in the Northern Hemisphere show up as regions of anomalous reflectivity (Fig. 2g). Except for these regions, parts of the Asian monsoon area, and a small region over the pole, the Southern Hemisphere reveals large negative values of $\Delta[F_{\text{atm}}(\lambda, \varphi) - G_{\text{atm}}(\lambda, \varphi)]$ poleward of 30° (Fig. 2g). This dominance is especially symmetric in the latitude band between 45° and 60° (between northern Spain and southern Greenland) and associated with the pronounced minimum in zonal mean values (Fig. 1) discussed above. This is mainly related to relatively large cloudiness in the southern storm tracks.

Figures 2a and 2g further document how the pattern of $\Delta[F_{\text{atm}}(\lambda, \varphi) - G_{\text{atm}}(\lambda, \varphi)]$ determines that of $\Delta F(\lambda, \varphi)$. Differences between the two patterns are mostly evident over the continents, where there is less cloud masking, and cloud-free asymmetries from land (primarily) and the aerosol (secondarily) are more pronounced (Figs. 2d,f). Near the poles, clouds increase reflectance in the NH, whose pole is apparently cloudier, but not so much as to compensate for the increased brightness of the land ice over Antarctica (Figs. 2d,g).

b. CMIP simulations

In this section, we explore to what extent general circulation models, as sampled across the three recent major phases of the Coupled Model Intercomparison Project, capture the observed contributions to the hemispheric asymmetry. In particular, we are interested in the extent to which the modeled clouds act to compensate for the reflection asymmetries due to the hemispherical asymmetric distribution of continents and aerosols, as shown above for CERES observations. We will demonstrate that the CMIP models at least partly compensate clear-sky asymmetries, and that, while over the CMIP phases, the patterns of the model mean biases of the various components of I are unchanged, their amplitude decreases

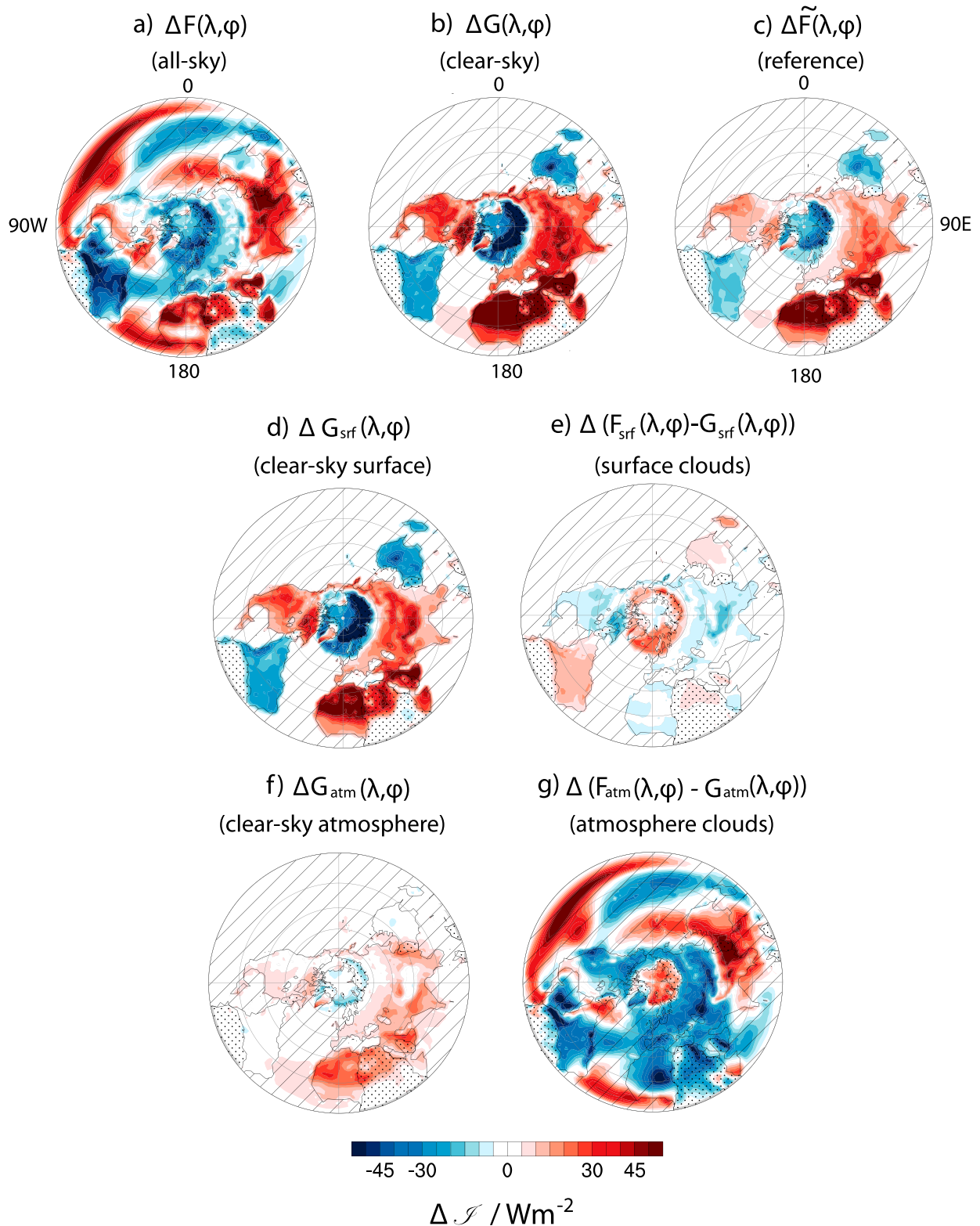


FIG. 2. North polar projection maps of NH – SH differences for CERES TOA SW upward radiation [$\Delta \mathcal{F}(\lambda, \varphi)$]: (a) all-sky [$\Delta F(\lambda, \varphi)$], (b) clear-sky [$\Delta G(\lambda, \varphi)$], (c) reference [$\Delta \tilde{F}(\lambda, \varphi)$], (d) clear-sky surface [$\Delta G_{\text{srf}}(\lambda, \varphi)$], (e) surface clouds [$\Delta F_{\text{srf}}(\lambda, \varphi) - \Delta G_{\text{srf}}(\lambda, \varphi)$], (f) clear-sky atmosphere [$\Delta G_{\text{atm}}(\lambda, \varphi)$], and (g) atmosphere clouds [$\Delta F_{\text{atm}}(\lambda, \varphi) - \Delta G_{\text{atm}}(\lambda, \varphi)$]. Hatching and stippling respectively mark regions covered by ocean and land in both hemispheres.

TABLE 3. Mean hemispheric differences $\Delta\mathcal{F}$ (NH – SH) of TOA SW upward radiation for CERES and CMIP model means, and RMSE w.r.t. CERES for CMIP (W m^{-2}).

	$\Delta\mathcal{F}$			$\sqrt{\mathcal{F}_{\text{CERES}}^2 - \mathcal{F}_{\text{CMIP}}^2}$			
	CERES	CMIP6	CMIP5	CMIP3	CMIP6	CMIP5	CMIP3
F	0.09	0.96	1.31	0.65	9.02	11.52	14.03
G	6.15	6.48	6.02	6.76	6.10	7.31	9.41
\tilde{F}	3.96	4.30	3.96	4.08	3.40	4.32	5.94
F_{srf}	2.25	2.81	2.88	3.49	3.66	4.39	5.82
G_{srf}	2.04	3.98	3.85	4.52	5.43	6.35	7.71
F_{atm}	-2.16	-1.85	-1.58	-2.84	9.65	11.97	14.69
G_{atm}	4.11	2.51	2.16	2.24	3.28	3.62	4.56

slightly. We further show that systematic (multimodel mean) biases in ΔF can mostly be attributed to an insufficient compensation by asymmetric clouds. In general, the individual models are largely consistent with the multimodel mean biases, but there is also a considerable spread among the GCMs of one CMIP phase.

1) HEMISPHERIC AVERAGES

On average, CMIP models tend to hemispherically symmetrize reflected SW radiation. However, the symmetry is not as perfect as for CERES, and there is no systematic reduction across the CMIP phases in this overall bias. In addition, the spread among the models within one CMIP phase is large. For the model means and their standard deviations, we find $\Delta F = 0.96 \pm 8.51 \text{ W m}^{-2}$ (CMIP6), $1.31 \pm 12.10 \text{ W m}^{-2}$ (CMIP5), and $0.65 \pm 7.65 \text{ W m}^{-2}$ (CMIP3), in comparison with 0.09 W m^{-2} for CERES (Table 3). The simulated reference asymmetry $\Delta\tilde{F}$ ($4.30 \pm 3.58 \text{ W m}^{-2}$ for CMIP6, $3.96 \pm 5.15 \text{ W m}^{-2}$ for CMIP5, and $4.08 \pm 3.85 \text{ W m}^{-2}$ for CMIP3) as compared with 3.96 W m^{-2} for CERES also shows no systematic improvement, as the largest difference in comparison with CERES is analyzed for the most recent generation of models. However, differences and standard deviations in $\Delta\tilde{F}$ are substantially less than the corresponding numbers in ΔF across all models and across all CMIP phases (Figs. 3a,c). This indicates that the masking effect by symmetric clouds is in better agreement with the observations than is the compensation effect ($\Delta F - \Delta\tilde{F}$), even after accounting for the fact that the latter is larger than the masking effect.

The individual GCMs compensate their corresponding $\Delta\tilde{F}$ to different degrees. Figure 4 plots ΔF versus $\Delta\tilde{F}$ for each GCM, CERES, and the multimodel mean for each phase of CMIP. The CERES marker (black dot in Fig. 4) appears near the vertical gray line, which represents exact symmetry, that is, $\Delta F = 0$. Indicated in the figure are the boundaries which demarcate which models enhance, undercompensate, or overcompensate the reference asymmetry. Across all three CMIP phases, it is rare for a model to enhance the hemispheric asymmetry. The vast majority show some compensation, but as a rule, the compensation is too weak. Thus, the CMIP mean marker (red dot in Fig. 4) appears in the section of undercompensation. Models for which the markers lie

between the two dashed lines of Fig. 4 have an absolute ΔF smaller than 50% of their $\Delta\tilde{F}$. In CMIP6, this is the case for 63% of the models, for 73% in CMIP3, but only 33% in CMIP5, again indicative of the lack of systematic improvement. Figure S2 in the online supplemental material shows that the individual model biases calculated for two 10-yr sub-periods of the CMIP6 simulations are very similar to the full 20-yr period analyzed for Fig. 4, which shows the robustness of the results.

Because of the tendency of some models to overcompensate for cloud-free albedo asymmetries, multimodel mean biases of clear-sky asymmetries ΔG tend to be smaller than for any individual model across CMIP phases (see Table 3 for all numbers in this and the next paragraph). The maximum bias of about 10% of the CERES clear-sky asymmetry occurred in CMIP3. The relative and absolute biases of the surface (ΔG_{srf}) and atmospheric (ΔG_{atm}) contributions to the clear-sky asymmetry are, however, much larger. The clear-sky surface contribution is close to 4 W m^{-2} in all CMIP phases, which is about twice the CERES value. This bias is, however, to a large extent compensated by the atmospheric (i.e., aerosol) contribution (ΔG_{atm}) to this asymmetry, which is between 1.6 and 1.95 W m^{-2} too small in the CMIP phases relative to CERES. These too-small ΔG_{atm} values could be due to insufficient mineral dust, an overly symmetric distribution of anthropogenic aerosol, or too much sea salt over the southern oceans.

The large bias of ΔG_{srf} leads to a too-large asymmetry of the total surface contribution ΔF_{srf} (by $\sim 2.85 \text{ W m}^{-2}$ in CMIP5 and CMIP6 and 3.49 W m^{-2} in CMIP3, as compared with 2.25 W m^{-2} in CERES), although it is attenuated by clouds [$\Delta(F_{\text{srf}} - G_{\text{srf}})$]. In CMIP5 and CMIP6, a slightly too weak negative asymmetry of the atmospheric contribution ΔF_{atm} adds to the biases of the total all-sky difference ΔF . The relatively small biases of ΔF_{atm} of less than 0.70 W m^{-2} are, however, again the result of compensating larger biases: the above-mentioned too-weak positive clear-sky contributions ΔG_{atm} (biases between -1.95 W m^{-2} in CMIP5 and -1.60 W m^{-2} in CMIP6) and the too-weak negative cloud contributions $\Delta(F_{\text{atm}} - G_{\text{atm}})$ (biases between 1.19 W m^{-2} in CMIP3 and 2.52 W m^{-2} in CMIP5).

Many of the individual models share the structural biases of the multimodel mean. Figure 3 shows, however, that there is also a large spread in individual radiation contributions, as presented in the right-hand parts of the figure's panels, representing the total means of the hemispheric difference for the individual models. The spread is largest for $\Delta(F_{\text{atm}} - G_{\text{atm}})$, which measures clouds, and ΔF . The question arises of whether the biases of the various contributions of the individual GCMs correlate with ΔF . Actually, this is only the case for $\Delta(F_{\text{atm}} - G_{\text{atm}})$. CMIP6 not only shows a very strong correlation between the biases of $\Delta(F_{\text{atm}} - G_{\text{atm}})$ and ΔF with only a few outliers but also a regression slope of almost 1 (Fig. 5). This means that a bias of $\Delta(F_{\text{atm}} - G_{\text{atm}})$ is accompanied with an almost equal bias of ΔF . Thus, we conclude that the biases of the individual ΔF are mainly due to biases of $\Delta(F_{\text{atm}} - G_{\text{atm}})$, that is, clouds. For CMIP5 and CMIP3, the results are a bit less clear. Here, the slopes are smaller than

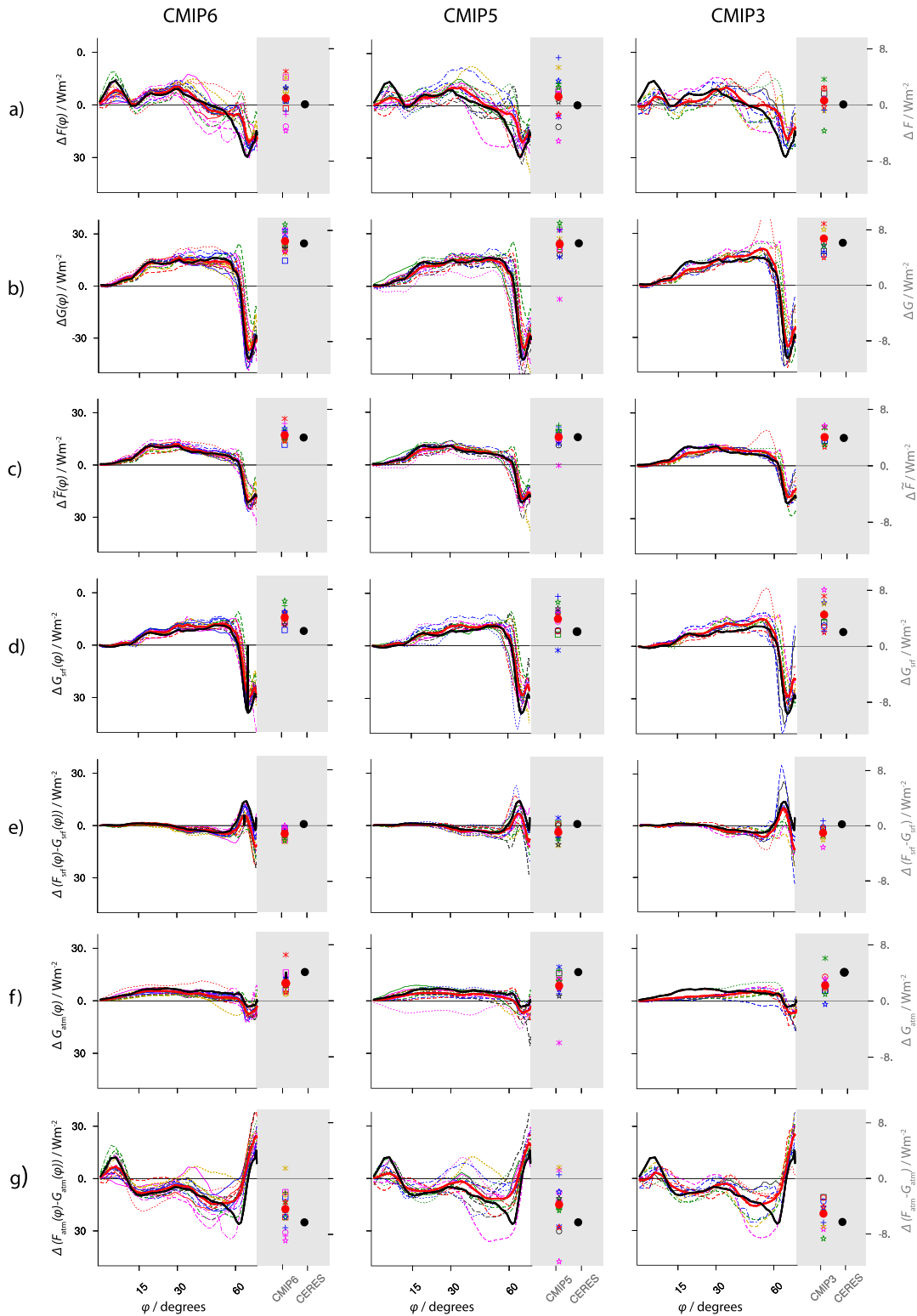


FIG. 3. TOA SW upward radiation differences (NH – SH): zonal means [$\Delta\mathcal{T}(\varphi)$; left part of each panel] and total means ($\Delta\mathcal{T}$); right part of each panel] for CERES and (left) CMIP6, (center) CMIP5, and (right) CMIP3 for (a) all-sky [$\Delta F(\varphi)$], (b) clear-sky [$\Delta G(\varphi)$], (c) reference [$\Delta\tilde{F}(\varphi)$], (d) clear-sky surface [$\Delta G_{\text{srf}}(\varphi)$], (e) surface clouds [$\Delta F_{\text{srf}}(\varphi) - \Delta G_{\text{srf}}(\varphi)$], (f) clear-sky atmosphere [$\Delta G_{\text{atm}}(\varphi)$], and (g) atmosphere clouds [$\Delta F_{\text{atm}}(\varphi) - \Delta G_{\text{atm}}(\varphi)$]. The red dot and the red thick line represent the CMIP mean. The black dot and the black thick line represent CERES. See Fig. S1 in the online supplemental material for line styles and markers of the individual GCMs.

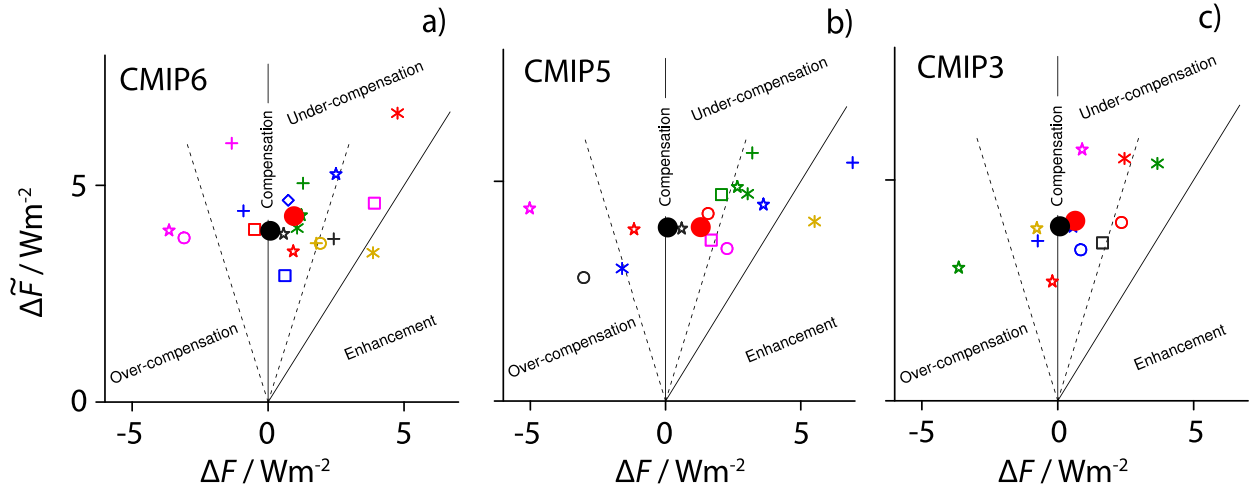


FIG. 4. Hemispheric mean differences of TOA SW upward radiation for the individual GCMs: all-sky (ΔF) vs reference assuming symmetric clouds ($\Delta \bar{F}$) for (a) CMIP6, (b) CMIP5, and (c) CMIP3. The solid vertical line represents total hemispheric symmetry of reflected radiation, the solid line on the right of each panel separates the sections of enhancement and undercompensation. The area to the left of the vertical line represents overcompensation, and the two dashed lines compose the section where the amount of ΔF is less than 50% of $\Delta \bar{F}$. Note that for CMIP5 only 15 GCMs are shown because one reveals a negative $\Delta \bar{F}$. The red dot represents the CMIP mean, and the black dot represents CERES. See Fig. S1 in the online supplemental material for markers of the individual GCMs.

one, indicating that other biases contribute to ΔF biases. In this respect, the CMIP6 models better match the observations than do the CMIP3 and CMIP5 models, notwithstanding that the dominant bias, that is, that associated with $\Delta(F_{\text{atm}} - G_{\text{atm}})$, is unchanged.

2) LATITUDE DEPENDENCE

The left-hand parts of the panels of Fig. 3 show the zonally averaged hemispheric differences [$\Delta I(\varphi)$] for CERES (thick black line), the CMIP multimodel means (thick red line), and the individual models. Overall, the GCMs show similar latitude dependence as CERES, which is the case for all

investigated quantities and all CMIP phases but is best in the case of CMIP6. For $\Delta F(\varphi)$, from the subtropics up to the mid-latitudes, there is a strong correspondence between the CERES and the CMIP mean curves. Clearly reduced amounts relative to CERES are found near the equator and around 60° . Because of their opposite signs, these zonal mean biases compensate to the overall small ΔF biases (Table 3). The effect of clouds as measured by $\Delta[F_{\text{atm}}(\varphi) - G_{\text{atm}}(\varphi)]$ reveals a similar behavior as $\Delta F(\varphi)$, with negative biases in the tropics and positive biases around 60° , while between these areas, we find a nearly perfect fit between the curves, at least for the CMIP6 multimodel mean. Thus, CMIP and CERES show the same behavior in that in the tropics, $\Delta[F_{\text{atm}}(\varphi) - G_{\text{atm}}(\varphi)]$

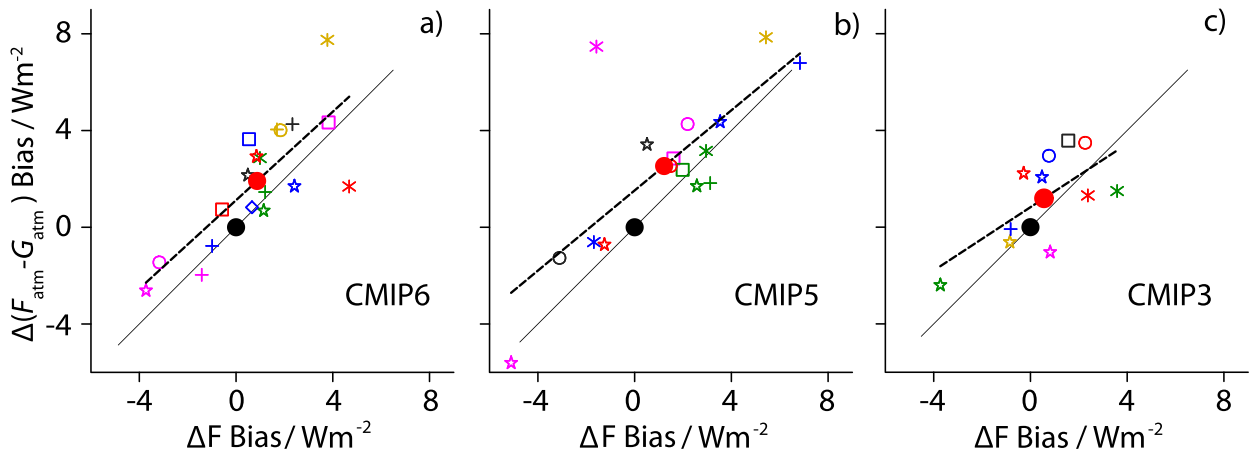


FIG. 5. Biases of hemispheric mean differences of TOA SW upward radiation for the individual GCMs w.r.t. CERES: all-sky (ΔF) v atmosphere clouds [$\Delta(F_{\text{atm}} - G_{\text{atm}})$] for (a) CMIP6, (b) CMIP5, and (c) CMIP3. The solid line represents equality. The dashed line results from a linear regression of the points marking the individual GCMs. The red dot represents the CMIP mean, and the black dot represents CERES. See Fig. S1 in the online supplemental material for markers of the individual GCMs.

enhances clear-sky asymmetries, while in the polar and subpolar areas, the compensation occurs. However, this phenomenon is more pronounced for CERES than for CMIP. As found for CERES, the CMIP curves for $\Delta G(\varphi)$, $\Delta \tilde{F}(\varphi)$, $\Delta G_{\text{srf}}(\varphi)$, and $\Delta G_{\text{atm}}(\varphi)$ show some similarities (Figs. 3b–d,f). Except for some outliers, the model spread is smaller here when compared with $\Delta F(\varphi)$ and $\Delta[F_{\text{atm}}(\varphi) - G_{\text{atm}}(\varphi)]$ (Figs. 3a,g).

3) REGIONAL DISTRIBUTION

The mean biases of hemispheric differences as discussed above show no clear improvement over the CMIP phases. However, the root-mean-square errors (RMSEs) of the grid-point differences do. The ΔF RMSE continuously decreases from about 14 W m^{-2} in CMIP3 to about 9 W m^{-2} in CMIP6 (Table 3). These improvements are also clearly visible in maps of $\Delta F(\lambda, \varphi)$ biases of the CMIP model means with respect to CERES data (Fig. 6a, right three columns). Nearly everywhere, the biases are reduced over the CMIP phases. This is the case not only for $\Delta F(\lambda, \varphi)$ but for almost all $\Delta I(\lambda, \varphi)$, with the exception of $\Delta[F_{\text{srf}}(\lambda, \varphi) - G_{\text{srf}}(\lambda, \varphi)]$, which remains almost unchanged (Fig. 6). These improvements may reflect a systematic improvement in the representation of the mean patterns of cloudiness, which, we speculate, may be the result of models moving to higher resolution, which, in turn, allows the models a better representation of orographic features and surface gradients known to be important for the distribution of clouds and aerosols. To test this hypothesis, we compare higher- and lower-resolution CMIP6 models and show that the higher-resolution models, on average, have smaller biases than lower-resolution models (Fig. S3 in the online supplemental material).

At a glance, all the anomaly maps in Fig. 6 (right three panels) show inverse patterns when compared with the CERES maps (left panel). This indicates that CMIP models generally underestimate the regional hemispheric differences of reflected radiation. The inverse pattern is especially pronounced for the all-sky reflection difference $[\Delta F(\lambda, \varphi)]$ in the tropical Pacific and Atlantic areas, where, however, a clear bias reduction also is found across the CMIP phases. Also, between the higher latitudes of 60° and 75° , we find an inverse pattern when compared with CERES. Here, the biases are more persistent across the CMIP phases (Fig. 6a).

Continuous improvements across the CMIP phases are also found for the clear-sky reflection differences $\Delta G(\lambda, \varphi)$, especially in the subtropical band of the Eastern hemisphere (Fig. 6b). Assuming realistic reflection over the ocean, for the Sahara region, the asymmetries suggest too little reflection relative to CERES. For Australia, reflection is too large in CMIP5 and CMIP3. For the Tibetan plateau, too-large reflection is simulated persistently over all phases. This may be related to an average overestimation of surface albedo in this region, as diagnosed for CMIP5 models by An et al. (2022). Relatively unchanged biases are found around 65° , where the high negative values of CERES are similarly underestimated in all CMIP phases. This result is consistent with the zonal means shown in Fig. 3b. All $\Delta \mathcal{S}(\lambda, \varphi)$ bias patterns show some spatial compensation, that is, areas with both positive and negative biases. In the case of the aerosol contribution

$G_{\text{atm}}(\lambda, \varphi)$, however, the difference between the hemispheres is underestimated in all CMIP phases, especially in almost all land areas, leading to the relatively high hemispheric mean biases reported above (Fig. 6f).

For CERES, we mentioned a strong similarity between the patterns of $\Delta F(\lambda, \varphi)$ and the atmosphere-cloud reflection difference $\{\Delta[F_{\text{atm}}(\lambda, \varphi) - G_{\text{atm}}(\lambda, \varphi)]\}$ (Figs. 6a,g). This is also found for the corresponding multimodel mean bias patterns of CMIP; that is, as for the $\Delta F(\lambda, \varphi)$ bias pattern, we observe negative $\Delta[F_{\text{atm}}(\lambda, \varphi) - G_{\text{atm}}(\lambda, \varphi)]$ biases mainly in the equatorial Pacific and Atlantic, and positive biases in a belt around 65° (Figs. 6a,g). At all other latitudes, zonal compensation leads to negligible zonal mean biases, most strikingly for CMIP6 (see Figs. 3a,g). Thus, the equatorial oceans and the subpolar regions are not only important areas for the compensation of the clear-sky asymmetry in both, models and observations, but also the hemispheric mean model biases are dominated by these areas.

4) ATTRIBUTION TO CLOUD BIASES

In the previous section, we discussed that cloud contributions in the tropics enhance the asymmetry of the reference reflected radiation, while the compensation is mainly provided by extratropical clouds poleward of about 60° . Furthermore, we identified that these two regions are also responsible for the main biases of CMIP models. Here, we will attribute the biases to cloud biases. Figures 7a–c shows $F(\varphi)$ biases with respect to CERES (the CMIP mean is represented by the red, solid, thick line). Positive biases occur in the tropics on both sides of the equator. In contrast, poleward of about 60° , the biases are negative in the south, but moderately positive in the north. This means for the asymmetries that the tropical biases partly cancel each other while the extratropical biases accumulate, consistent with the finding by Jönsson and Bender (2022) that extratropical biases largely scale biases in all-sky ΔF . This behavior is true for the multimodel mean and many individual GCMs. However, there is a considerable spread across models and, especially, a few CMIP3 and CMIP5 models show very different biases.

The biases of the zonally averaged total cloud contribution to the reflected SW radiation $[F(\varphi) - G(\varphi)]$ (Figs. 7g–i) are very similar to the all-sky biases, confirming that, indeed, clouds are the major source of the biases. The tropical biases of the total cloud contributions are even larger than those of the all-sky reflection $F(\varphi)$ because of weakly negative tropical clear-sky biases (Figs. 7d–f), but again, they largely cancel with respect to hemispheric asymmetries. Besides that, the clear-sky biases are notable only near the poles. Also, the spread of CMIP model biases of $F(\varphi)$ can be mainly attributed to the spread of the biases of the cloud contributions.

5. Summary and discussion

CERES observations show an almost-perfect hemispheric symmetry of reflected SW radiation. The hemispheric difference is indistinguishable from zero, although the land surfaces and atmospheric aerosols introduce an asymmetry of 6.15 W m^{-2} . We analyze the role of clouds in this process

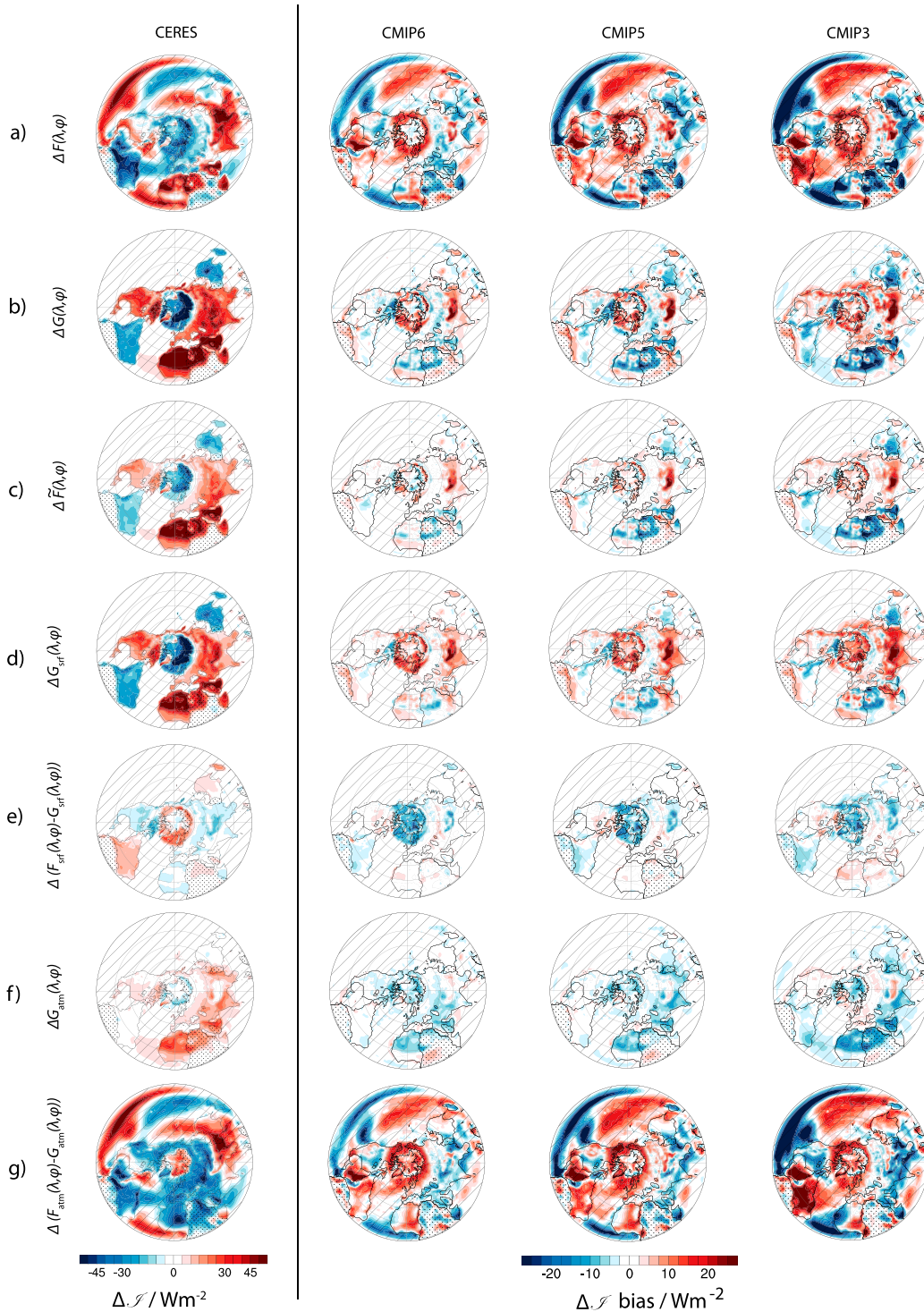


FIG. 6. North polar projection maps of NH – SH differences for (left) CERES and (left center) CMIP6, (right center) CMIP5, and (right) CMIP3 biases w.r.t. CERES of TOA SW upward radiation $[\Delta \mathcal{F}(\lambda, \varphi)]$: (a) all-sky $[\Delta F(\lambda, \varphi)]$, (b) clear-sky $[\Delta G(\lambda, \varphi)]$, (c) reference $[\Delta \tilde{F}(\lambda, \varphi)]$, (d) clear-sky surface $[\Delta G_{\text{srf}}(\lambda, \varphi)]$, (e) surface clouds $[\Delta F_{\text{srf}}(\lambda, \varphi) - \Delta G_{\text{srf}}(\lambda, \varphi)]$, (f) clear-sky atmosphere $[\Delta G_{\text{atm}}(\lambda, \varphi)]$, and (g) atmosphere clouds $[\Delta F_{\text{atm}}(\lambda, \varphi) - \Delta G_{\text{atm}}(\lambda, \varphi)]$. Hatching and stippling respectively mark regions covered by ocean and land in both hemispheres.

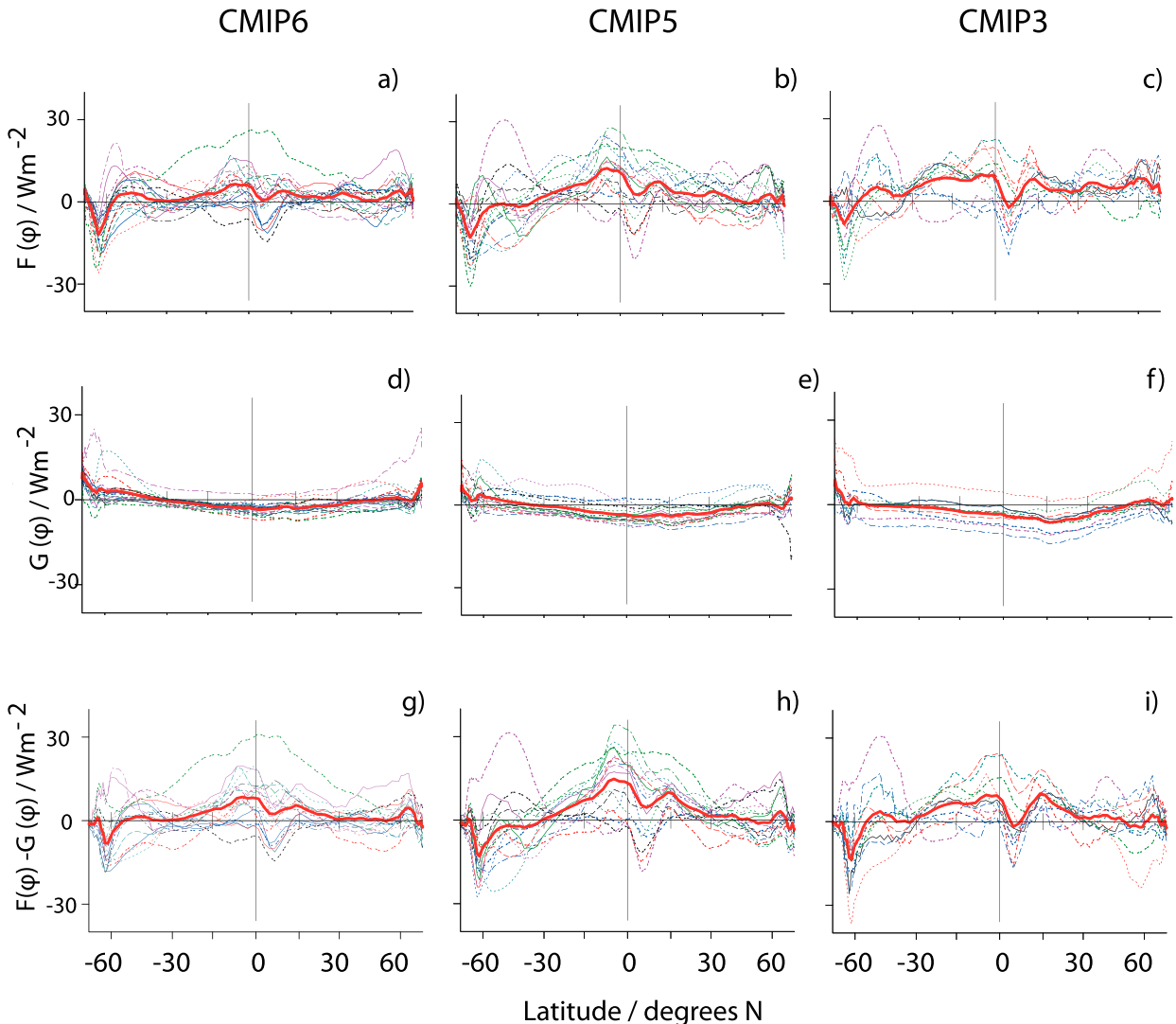


FIG. 7. Zonal mean biases of (left) CMIP6, (center) CMIP5, and (right) CMIP3 TOA SW radiation components w.r.t. CERES: (a)–(c) all sky $[F(\varphi)]$, (d)–(f) clear-sky $[G(\varphi)]$, and (g)–(i) total cloud contributions $[F(\varphi) - G(\varphi)]$. The red solid line represents the CMIP mean (see Fig. S1 in the online supplemental material for line styles of the individual GCMs).

and to what extent general circulation models in the most recent three major CMIP phases represent the observed features. We assess the contributions of the surface, aerosols, and, especially, clouds to the reflection of solar radiation, following the diagnostic framework introduced by Donohoe and Battisti (2011). In addition, we followed Voigt et al. (2013) and calculated a reference reflection asymmetry, defined as the clear-sky asymmetry masked by hemispherically symmetric clouds. By these means, we analyze the GCMs' performances in the compensation of the reference reflection asymmetry.

From the CERES data, we confirm the result of previous satellite data studies that extratropical clouds play a crucial role in the compensation of the clear-sky asymmetry. Over the ocean, extratropical clouds in the Southern Hemisphere reflect more sunlight than over similar regions in the Northern

Hemisphere, resulting in a negative reflection difference between the corresponding northern and southern latitudes. This was already concluded by Datsieris and Stevens (2021) and has recently been attributed to the larger storminess of the southern storm tracks (Hadas et al. 2023; Blanco et al. 2023). The asymmetry of tropical clouds actually enhances the reference asymmetry, as previously shown by Bender et al. (2017) and Jönsson and Bender (2022). Thus, extratropical cloud asymmetries not only balance the reference asymmetry but also the additional asymmetry introduced by tropical clouds. We additionally identify that this positive tropical asymmetry contribution originates predominantly from the east Pacific and Atlantic regions. The west Pacific hardly contributes to the asymmetry, as over the warm pool, deep precipitating clouds are distributed more symmetrically about the equator.

In contrast to our results, Voigt et al. (2014) found in aquaplanet simulations that an idealized hemispheric surface albedo difference would be partly compensated by a shift of the ITCZ leading to more clouds in the hemisphere with the darker surface. This is clearly not what is happening in the observations. The search for a hemispheric compensation mechanism is still open, but our work joins a growing number of studies that point to an important role for extratropical clouds. As the extratropical circulation is influenced by land-ocean distributions, it is clear that the hemispheric asymmetry of this distribution not only introduces the clear-sky asymmetry but also plays an important role in its compensation.

Overall, CMIP multimodel means show similar SW radiation reflection properties as observed by CERES. For all three CMIP phases, model means show all-sky hemispheric asymmetries that are of the order of 1 W m^{-2} and only 15%–33% of the reference asymmetries, that is, asymmetries expected given symmetric clouds. Thus, we conclude that GCMs generally adjust clouds at least partly to compensate the asymmetry. The relatively small multimodel mean biases are, however, the result of averaging over much larger compensating biases of the individual models. For all CMIP phases, the multimodel standard deviation of the all-sky asymmetry is about 10 times the mean value. Surprisingly, the mean all-sky asymmetry is smallest for the average of the oldest GCMs. While for 73% of the CMIP3 GCMs, the absolute value of the asymmetry is smaller than half of the reference, this is true for only 63% of the CMIP6 and 33% of the CMIP5 GCMs. In this sense, we confirm results of Stephens et al. (2015) that CMIP5 climate models do only show a weak tendency to symmetrize. However, this tendency is somewhat larger in the other two CMIP phases. Our findings also confirm the results of Voigt et al. (2013) that among the CMIP3 GCMs, the extent of compensation widely differs. However, the latter study did not discuss the multimodel means, which are shown here to provide only relatively small biases.

These numbers seem to indicate no improvement over CMIP phases, that is, there is no systematic reduction of the mean hemispheric asymmetry of all-sky reflection going from CMIP3, to CMIP5, and CMIP6. A comparison of high- and low-resolution CMIP6 models suggests that this arises as a result of progressive improvements in resolution. However, this is different for the spatial patterns of hemispheric differences. RMSEs of the all-sky reflection differences $[\Delta F(\lambda, \varphi)]$ and of almost all individual contributions $\Delta I(\lambda, \varphi)$ to $\Delta F(\lambda, \varphi)$ are clearly reduced going from CMIP3 to CMIP5 and CMIP6. However, the remaining bias patterns show that even in CMIP6, the relatively small hemispheric mean asymmetry is the result of compensating regional biases. To the extent the models are improving, they are doing so because of smaller regional biases, but also partly because of compensating biases. The reflected radiation difference is less positive than that observed by CERES in the tropics and less negative in the high latitudes (Figs. 3 and 6). The bias pattern of the hemispheric all-sky difference $\Delta F(\lambda, \varphi)$ is strongly related to the cloud contribution $\Delta[F_{\text{atm}}(\lambda, \varphi) - G_{\text{atm}}(\lambda, \varphi)]$, which emphasizes the importance of clouds not only for the

compensation of hemispheric clear-sky asymmetries but also for the remaining compensation biases of the GCMs.

In the northern high latitudes, clouds reflect (in general) too much, and in the southern high latitudes too little, radiation. These two issues add up to the hemispheric difference bias. In the tropics, the cloud reflection biases are positive north and south of the equator, but only partly compensate because they are larger in the south. This too-high reflection south of the equator can be expected due to the double ITCZ, which is a longstanding problem of GCMs (e.g., Lin 2007; Tian and Dong 2020).

An unexpected result of our analysis is the model biases in the different contributions to the clear-sky asymmetry. The total clear-sky hemispheric differences lie between 6 and 7 W m^{-2} in CERES data and CMIP multimodel means of all phases. However, while CERES indicates that the atmospheric (aerosol) contribution to this is about 2 W m^{-2} larger than the surface contribution, the relation is almost opposite in the GCM means. These sorts of systematic biases in what amounts to an imposed forcing were shown by Haywood et al. (2016) to lead to circulation biases. Hence, if models of the type analyzed here are to be used to study hemispheric albedo biases, it would be helpful to understand the origin of the clear-sky differences between the models and CERES and, if they are true biases, to what extent they condition systematic cloud biases.

Although our analysis does not bode well for identifying compensation mechanisms from the output of existing CMIP models, it does suggest that these asymmetries reflect coherent differences in the large-scale circulations and, as such, provide a critical test for those developing the models. Certainly, to build confidence in the ability of models to distinguish the clouds of the present climate from those of a warmer climate, one would like models to be able to explain what drives differences in the clouds of the Northern Hemisphere as compared with the Southern Hemisphere. Even in the absence of meeting this tall order, CMIP class models are amenable for testing cloud-controlling factors that couple to large-scale circulations in ways that enhance or mute hemispheric albedo asymmetries and which would be more difficult to introduce in more physically based models. Targeted experimentation of this kind might help shed light on whether the observed absence of hemispheric asymmetry in reflected shortwave irradiances is a whim, rather than a way, of nature.

Acknowledgments. We acknowledge the CMIP3, CMIP5, and CMIP6 communities for providing the data of the climate models, which, for this study, were made available by the Deutsches Klimarechenzentrum (DKRZ). The figures were performed using the NCAR Command Language (version 6.6.2) (2019) from UCAR/NCAR/CISL/TDD (<https://doi.org/10.5065/D6WD3XH5>). We thank the two anonymous reviewers for the appraisal of our paper. We are grateful to Ulrike Niemeier at the Max Planck Institute for Meteorology for a careful internal review. This research was supported by the Max Planck Society for the Advancement of Science.

Data availability statement. The CERES EBAF Ed4.0 data were obtained online (<https://ceres.larc.nasa.gov/data>). CMIP data of this study were made available by the DKRZ.

REFERENCES

- An, Y., X. Meng, L. Zhao, Z. Li, S. Wang, L. Shang, H. Chen, and S. Lyu, 2022: Evaluation of surface albedo over the Tibetan Plateau simulated by CMIP5 models using in-situ measurements and MODIS. *Int. J. Climatol.*, **42**, 928–951, <https://doi.org/10.1002/joc.7281>.
- Arrhenius, S., 1896: On the influence of carbonic acid in the air upon the temperature of the ground. *London Edinburgh Dublin Philos. Mag. J. Sci.*, **41**, 237–276, <https://doi.org/10.1080/14786449608620846>.
- Bender, F. A.-M., A. Engström, R. Wood, and R. J. Charlson, 2017: Evaluation of hemispheric asymmetries in marine cloud radiative properties. *J. Climate*, **30**, 4131–4147, <https://doi.org/10.1175/JCLI-D-16-0263.1>.
- Blanco, J. E., R. Caballero, G. Datsersis, B. Stevens, S. Bony, O. Hadas, and Y. Kaspi, 2023: A cloud-controlling factor perspective on the hemispheric asymmetry of extratropical cloud albedo. *J. Climate*, **36**, 1793–1804, <https://doi.org/10.1175/JCLI-D-22-0410.1>.
- Datsersis, G., and B. Stevens, 2021: Earth's albedo and its symmetry. *AGU Adv.*, **2**, e2021AV000440, <https://doi.org/10.1029/2021AV000440>.
- Diamond, M., J. J. Gristey, J. E. Kay, and G. Feingold, 2022: On the rise and fall of Earth's strong clear-sky hemispheric albedo asymmetry. ESS Open Archive, 32 pp., <https://doi.org/10.1002/essoar.10511017.2>.
- Donohoe, A., and D. S. Battisti, 2011: Atmospheric and surface contributions to planetary albedo. *J. Climate*, **24**, 4402–4418, <https://doi.org/10.1175/2011JCLI3946.1>.
- Eyring, V., S. Bony, G. A. Meehl, C. A. Senior, B. Stevens, R. J. Stouffer, and K. E. Taylor, 2016: Overview of the Coupled Model Intercomparison Project phase 6 (CMIP6) experimental design and organization. *Geosci. Model Dev.*, **9**, 1937–1958, <https://doi.org/10.5194/gmd-9-1937-2016>.
- Hadas, O., G. Datsersis, J. Blanco, S. Bony, R. Caballero, B. Stevens, and Y. Kaspi, 2023: The role of baroclinic activity in controlling Earth's albedo in the present and future climates. *Proc. Natl. Acad. Sci. USA*, **120**, e2208778120, <https://doi.org/10.1073/pnas.2208778120>.
- Haywood, J. M., and Coauthors, 2016: The impact of equilibrating hemispheric albedos on tropical performance in the HadGEM2-ES coupled climate model. *Geophys. Res. Lett.*, **43**, 395–403, <https://doi.org/10.1002/2015GL066903>.
- Jönsson, A., and F. A.-M. Bender, 2022: Persistence and variability of Earth's interhemispheric albedo symmetry in 19 years of CERES EBAF observations. *J. Climate*, **35**, 249–268, <https://doi.org/10.1175/JCLI-D-20-0970.1>.
- Kato, S., and Coauthors, 2018: Surface irradiances of Edition 4.0 Clouds and the Earth's Radiant Energy System (CERES) Energy Balanced and Filled (EBAF) data product. *J. Climate*, **31**, 4501–4527, <https://doi.org/10.1175/JCLI-D-17-0523.1>.
- Lin, J.-L., 2007: The double-ITCZ problem in IPCC AR4 coupled GCMs: Ocean–atmosphere feedback analysis. *J. Climate*, **20**, 4497–4525, <https://doi.org/10.1175/JCLI4272.1>.
- Loeb, N. G., S. Kato, and B. A. Wielicki, 2002: Defining top-of-the-atmosphere flux reference level for Earth radiation budget studies. *J. Climate*, **15**, 3301–3309, [https://doi.org/10.1175/1520-0442\(2002\)015<3301:DTOTAF>2.0.CO;2](https://doi.org/10.1175/1520-0442(2002)015<3301:DTOTAF>2.0.CO;2).
- , B. A. Wielicki, D. R. Doelling, G. L. Smith, D. F. Keyes, S. Kato, N. Manalo-Smith, and T. Wong, 2009: Toward optimal closure of the Earth's top-of-atmosphere radiation budget. *J. Climate*, **22**, 748–766, <https://doi.org/10.1175/2008JCLI2637.1>.
- , and Coauthors, 2018: Clouds and the Earth's Radiant Energy System (CERES) Energy Balanced and Filled (EBAF) top-of-atmosphere (TOA) Edition-4.0 data product. *J. Climate*, **31**, 895–918, <https://doi.org/10.1175/JCLI-D-17-0208.1>.
- , H. Wang, F. G. Rose, S. Kato, W. L. Smith Jr., and S. Sun-Mack, 2019: Decomposing shortwave top-of-atmosphere and surface radiative flux variations in terms of surface and atmospheric contributions. *J. Climate*, **32**, 5003–5019, <https://doi.org/10.1175/JCLI-D-18-0826.1>.
- Meehl, G. A., C. Covey, T. Delworth, M. Latif, B. McAvaney, J. F. B. Mitchell, R. J. Stouffer, and K. E. Taylor, 2007: The WCRP CMIP3 multimodel dataset: A new era in climate change research. *Bull. Amer. Meteor. Soc.*, **88**, 1383–1394, <https://doi.org/10.1175/BAMS-88-9-1383>.
- Qu, X., and A. Hall, 2005: Surface contribution to planetary albedo variability in the cryosphere regions. *J. Climate*, **18**, 5239–5252, <https://doi.org/10.1175/JCLI3555.1>.
- Stephens, G. L., D. O'Brien, P. J. Webster, P. Pilewski, S. Kato, and J.-I. Li, 2015: The albedo of Earth. *Rev. Geophys.*, **53**, 141–163, <https://doi.org/10.1002/2014RG000449>.
- , M. Z. Hakuba, M. Hawcroft, J. M. Haywood, A. Behrangi, J. E. Kay, and P. J. Webster, 2016: The curious nature of the hemispheric symmetry of the Earth's water and energy balances. *Curr. Climate Change Rep.*, **2**, 135–147, <https://doi.org/10.1007/s40641-016-0043-9>.
- Stevens, B., and S. E. Schwartz, 2012: Observing and modeling Earth's energy flows. *Surv. Geophys.*, **33**, 779–816, <https://doi.org/10.1007/s10712-012-9184-0>.
- Taylor, K. E., R. J. Stouffer, and G. A. Meehl, 2012: An overview of CMIP5 and the experiment design. *Bull. Amer. Meteor. Soc.*, **93**, 485–498, <https://doi.org/10.1175/BAMS-D-11-00094.1>.
- Tian, B., and X. Dong, 2020: The double-ITCZ bias in CMIP3, CMIP5, and CMIP6 models based on annual mean precipitation. *Geophys. Res. Lett.*, **47**, e2020GL087232, <https://doi.org/10.1029/2020GL087232>.
- Voigt, A., B. Stevens, J. Bader, and T. Mauritsen, 2013: The observed hemispheric symmetry in reflected shortwave irradiance. *J. Climate*, **26**, 468–477, <https://doi.org/10.1175/JCLI-D-12-00132.1>.
- , —, —, and —, 2014: Compensation of hemispheric albedo asymmetries by shifts of the ITCZ and tropical clouds. *J. Climate*, **27**, 1029–1045, <https://doi.org/10.1175/JCLI-D-13-00205.1>.
- Vonder Haar, T. H., and V. E. Suomi, 1971: Measurements of the Earth's radiation budget from satellites during a five-year period. Part I: Extended time and space means. *J. Atmos. Sci.*, **28**, 305–314, [https://doi.org/10.1175/1520-0469\(1971\)028<0305:MOTERB>2.0.CO;2](https://doi.org/10.1175/1520-0469(1971)028<0305:MOTERB>2.0.CO;2).

Copyright of Journal of Climate is the property of American Meteorological Society and its content may not be copied or emailed to multiple sites or posted to a listserv without the copyright holder's express written permission. However, users may print, download, or email articles for individual use.